Olusegun Ilegbusi[1]
Department of Mechanical and Aerospace Engineering,
University of Central Florida,
4000 Central Florida Blvd.,
Orlando, FL 32826
e-mail: Ilegbusi@ucf.edu

Behnaz Seyfi
Department of Mechanical and Aerospace Engineering,
University of Central Florida,
4000 Central Florida Blvd.,
Orlando, FL 32826
e-mail: bsn@knights.ucf.edu

John Neylon
Department of Radiation Oncology,
University of California,
Los Angeles, CA 90095
e-mail: jneylon@mednet.ucla.edu

Anand P. Santhanam
Department of Radiation Oncology,
University of California,
Los Angeles, CA 90095
e-mail: ASanthanam@mednet.ucla.edu

Analytic Intermodel Consistent Modeling of Volumetric Human Lung Dynamics

Human lung undergoes breathing-induced deformation in the form of inhalation and exhalation. Modeling the dynamics is numerically complicated by the lack of information on lung elastic behavior and fluid–structure interactions between air and the tissue. A mathematical method is developed to integrate deformation results from a deformable image registration (DIR) and physics-based modeling approaches in order to represent consistent volumetric lung dynamics. The computational fluid dynamics (CFD) simulation assumes the lung is a poro-elastic medium with spatially distributed elastic property. Simulation is performed on a 3D lung geometry reconstructed from four-dimensional computed tomography (4DCT) dataset of a human subject. The heterogeneous Young's modulus (YM) is estimated from a linear elastic deformation model with the same lung geometry and 4D lung DIR. The deformation obtained from the CFD is then coupled with the displacement obtained from the 4D lung DIR by means of the Tikhonov regularization (TR) algorithm. The numerical results include 4DCT registration, CFD, and optimal displacement data which collectively provide consistent estimate of the volumetric lung dynamics. The fusion method is validated by comparing the optimal displacement with the results obtained from the 4DCT registration. [DOI: 10.1115/1.4031349]

Keywords: lung displacement, fusion algorithm, Tikhonov regularization, poro-elastic medium, flow-structure interaction (FSI)

1 Introduction

Respiratory motion is a potential source of error in the treatment of lung cancer using advanced therapies such as radiotherapy. Accurate prediction of lung deformation may aid targeted radiotherapy, ensuring precise tumor localization and underexposure of the surrounding healthy tissues to ionizing radiation [1]. Numerical modeling of human lung dynamics enables simulation and visualization of lung deformation based on underlying physics and physiology. However, the accuracy of numerical results may be affected by the inherent difficulties in computational modeling of a complicated system like the human lung. This paper presents a method to couple the results of computational modeling and 4D DIR method to improve accuracy of predicted lung deformation.

Recent advances in CT and magnetic resonance (MR) acquisition techniques have enabled direct dynamic imaging of respiratory motion. 4DCT imaging [2] and dynamic MR imaging [3] are used in radiation therapy to provide images of tumor and associated organ at different breathing phases. In addition, DIR methods and in particular, biomechanical modeling of the lung, facilitate precise estimation of lung tumor location during respiration. Biomechanical modeling has the advantage of being able to account for the physiology of the breathing process and the physical properties through the boundary conditions and material properties, in a dynamical model.

A number of studies have generally either considered the lung as a one-phase continuum and modeled its contact behavior [4,5] or modeled airflow in the lung and the mechanical coupling between the deformation of the solid tissue skeleton and the airflow [6,7]. However, even with advanced 4D imaging techniques and biomechanical modeling, errors and uncertainty in tracking lung anatomy during breathing are inevitable due to inherent limitation in imaging techniques and approximations in biomechanical modeling. The inherent difficulty in specifying exact boundary conditions, heterogeneous nonlinear nature of material properties, fluid–structure interaction between air and the poro-elastic lung tissue, and complex geometry, make biomechanical modeling a challenge. As a consequence, the necessary simplification and approximations associated with modeling may affect the accuracy of the predicted results.

A number of studies have considered the accuracy of deformation predicted by biomechanical model. Al-Mayah et al. [5] reported the average displacement errors of tumor location in the superior–inferior (SI) direction measured by landmarks to be 7.1 mm for linear elastic model without contact and −0.3 mm for hyperelastic model with contact. Brock et al. [8] reported an average displacement error of 1.7 mm in the SI direction. Werner et al. [9] predicted the average displacement error between 2 and 7 mm for landmarks at the trachea bifurcation, and between 1.1 mm and 4 mm for landmarks at the tumor location. Eom et al. [10] used a hyperelastic model to predict average displacement errors of 0.45 cm, 0.387 cm, 0.319 cm, and 0.204 cm at landmark locations for four different patients. Although the errors reported in these studies could be considered quite reasonable, the models utilized material constants obtained from experiments on animal tissue or cadaver, which are considered inadequate for human radiotherapy. In this study, we use the subject-specific material constants derived from real human patients and obtained an accuracy of about 3 mm for the selected landmarks in the lung. This value compares favorably with the desired accuracy of ± 3 mm based on lung radiotherapy application [11].

It should be remarked that our methodology is universally applicable to lungs with and without tumor. It is particularly well suited for lungs with tumor since it involves acquisition of data for the spatial material properties over the lung parenchyma with or without tumor.

We investigate the integration of CFD-based analysis and 4D DIR for consistent representation of human lung dynamics. Specifically, TR [12] is used to integrate quantitative image analysis and CFD simulation results in the human lung. The 4D DIR data is obtained by 4DCT image registration algorithm to estimate lung motion. The biomechanical modeling utilizes a

[1]Corresponding author.
Manuscript received October 16, 2014; final manuscript received July 27, 2015; published online September 7, 2015. Assoc. Editor: Guy M. Genin.

flow–structure interaction model to simultaneously solve the airflow equations and structural dynamics of the lung tissue. The lung is modeled as a poro-elastic medium with subject-specific heterogeneous elastic properties on a 3D geometry, reconstructed from 4DCT scan datasets of a human patient.

Sections 2–4 describe the methodology, followed by presentation of the results and subsequently, conclusion summarizing the findings of the study.

2 Materials and Methods

This section describes the fusion algorithm and provides some details on the formulation of the approach including the biomechanical model and imaging technique. The displacement obtained from the 4DCT algorithm is integrated with CFD solution using a fusion algorithm. The detailed description of each step involved is detailed below.

2.1 Fusion Algorithm. Let $\mathbf{f}_{opt}(\mathbf{x}), \mathbf{f}_{4DCT}(\mathbf{x})$, and $\mathbf{f}_{CFD}(\mathbf{x})$, respectively, represent optimal displacement, 4DCT (linear elastic model based) displacement, and CFD displacement vectors associated with a 3D anatomy. The optimal displacement is computed by fusing the displacement results obtained from 4DCT and biomechanical model. We now introduce the following regularization terms: (a) $\boldsymbol{\omega}(\mathbf{f}_{opt}(\mathbf{x}), \mathbf{f}_{CFD}(\mathbf{x}))$ representing the discrepancy between the optimal displacement vectors and the CFD-based displacement; and (b) $\boldsymbol{\varepsilon}(\mathbf{f}_{opt}(\mathbf{x}), \mathbf{f}_{4DCT}(\mathbf{x}))$ representing discrepancy between the optimal displacement and the linear elasticity model based (4DCT) deformation vectors. We first define an objective functional, $\mathbf{z}(\mathbf{f}_{opt}, \mathbf{f}_{4DCT}, \mathbf{f}_{CFD})$, which represents the discrepancy between the displacement obtained from 4DCT registration and the displacement obtained using the flow–structure interaction modeling. The formulation is given as

$$\mathbf{z}(\mathbf{f}_{opt}, \mathbf{f}_{4DCT}, \mathbf{f}_{CFD}) = \frac{1}{2}\,\alpha\,\boldsymbol{\varepsilon}\big(\mathbf{f}_{opt}(\mathbf{x}), \mathbf{f}_{4DCT}(\mathbf{x})\big) + \frac{1}{2}\boldsymbol{\omega}\big(\mathbf{f}_{opt}(\mathbf{x}), \mathbf{f}_{CFD}(\mathbf{x})\big) \quad (1)$$

where α is a regularization parameter. The regularization operator $\boldsymbol{\omega}(\mathbf{f}_{opt}(\mathbf{x}), \mathbf{f}_{CFD}(\mathbf{x}))$ is estimated by assuming that the space of functions to be Hilbert space, which has squared–integrable generalized derivative and $\boldsymbol{\varepsilon}(\mathbf{f}_{opt}(\mathbf{x}), \mathbf{f}_{4DCT}(\mathbf{x}))$ is defined as standard square error.

Substituting the definitions of $\boldsymbol{\omega}(\mathbf{f}_{opt}(\mathbf{x}), \mathbf{f}_{CFD}(\mathbf{x}))$ and $\boldsymbol{\varepsilon}(\mathbf{f}_{opt}(\mathbf{x}), \mathbf{f}_{4DCT}(\mathbf{x}))$ in Eq. (1), the objective functional, $\mathbf{z}(\mathbf{x})$, for a 3D domain is obtained as

$$\mathbf{z}(\mathbf{f}_{opt}, \mathbf{f}_{4DCT}, \mathbf{f}_{CFD}) = \frac{1}{2}\alpha\big[\mathbf{f}_{4DCT}(\mathbf{x}) - \mathbf{f}_{opt}(\mathbf{x})\big]^2 + \frac{1}{2}\big[\mathbf{f}_{opt}(\mathbf{x}) - \mathbf{f}_{CFD}(\mathbf{x})\big]^2 + \frac{1}{2}\{\nabla.\big[\mathbf{f}_{opt}(\mathbf{x}) - \mathbf{f}_{CFD}(\mathbf{x})\big]\}^2 \quad (2)$$

Using results obtained from the CFD solver and the results obtained from 4DCT registration, our ultimate goal is to seek numerical solution to minimize Eq. (2) as described below.

The computational complexity of Eq. (2) is implicitly related to the linear deformation model parameters and the CFD porosity parameters. Solving for a uniform material distribution for both of these systems is straightforward but too simplistic for representing the lung anatomy. A heterogeneous distribution of both the elastic parameters in the linear deformation model and the porosity parameters in the CFD model is critical for predicting accurate results. However, such a distribution of parameters will lead to a very complex system to solve. We now present a mechanism that simplifies the minimization problem in such a way that accounts for the heterogeneous nature of the lung elasticity and porosity.

Finite-element analysis is used to obtain the numerical solution of the objective functional, Eq. (2). For each element, the minimum of the objective functional can be obtained by differentiating the equation with respect to nodal values in that specific element. The numerical solution of the objective functional is detailed in the Appendix.

2.2 4DCT Registration Using Optical Flow ($\mathbf{f}_{4DCT}$). As explained in Sec. 2.1, the deformation values obtained from the 4DCT registration ($\mathbf{f}_{4DCT}$) are used as the input to the fusion algorithm. This section describes the registration method used to obtain the $\mathbf{f}_{4DCT}$ values.

Using the 4DCT data registration algorithm the motion of each 3D voxel at the end-expiration 3D volume data is estimated by searching for and locating a corresponding voxel in another 3D volume at a different breathing phase. An optical flow motion estimation algorithm was used for the registration based on local Taylor series approximation [13].

One of the limitations of the optical flow method as applied to estimating the 3D organ motion is the low sensitivity to variations in regional motion. In order to improve the accuracy of the optical flow algorithm, we used a multilevel, multiresolution optical flow method [2], which computed optical flow between two 3D volumes at low resolution, propagated the result to the higher resolution volume, and subsequently to the original resolution volume data. In this approach, the organ anatomy was divided into four parts: (1) lung outline, (2) large capillaries, (3) small capillaries, and (4) parenchyma. At each level of anatomy, a multilevel, multiresolution optical flow registration was used to compute the 4D organ motion of that anatomy and integrated into the next level. The four anatomical parts are semi-automatically separated using a seed-based region-growth algorithm. The motion consistency during the registration process is enabled by the thin plate splines applied at the anatomical boundaries [14].

2.3 CFD Model Analysis ($\mathbf{f}_{CFD}$). This section describes the different steps involved in CFD modeling of spatial lung displacement ($\mathbf{f}_{CFD}$). It considers the heterogeneity of the elasticity of lung tissue. The presence of vessels, bronchial tree and tumor (in the case of cancerous lung), creates inhomogeneity in the lung material properties. This inhomogeneity is represented by spatially distributed properties.

2.3.1 Reconstruct 3D Geometry of Real Human Lung From 4DCT Scan Dataset. 4DCT scans of the lung are obtained from a specific patient at the UCLA Department of Radiation Oncology, Los Angeles, CA. The dataset constitutes a sequence of 3DCT scans representing the volumetric lung anatomy at different air volumes and pressure–volume curves. The 4DCT scan dataset provides roughly 255 image slices (one slice per mm) of the lung. The resolution of each slice is 512×256 mm^2. The images are processed using the MIMICS software [15] to reconstruct the surface geometry of the lung.

2.3.2 Generate Computational Meshes in the Reconstructed Lung Geometry. The surface of the lung obtained after image processing is used as input to the 3-MATIC software [16]. This software is used to correct the typical errors associated with data transfer from a 3D digitization session, including missing data and extraneous parts. The surface of the lung is meshed with three-node triangular computational elements and used to generate a finite element discretization in the interior. Four-node-tetrahedral elements are used for volume discretization. A total of 37,752 surface meshes and 140,164 volume meshes are used for the left lung, while the corresponding values for the right lung are 38,298 and 279,181. Figures 1(*a*) and 1(*b*) show the reconstructed 3D geometry for the left and right lungs, respectively.

2.3.3 Governing Equations. The biomechanical model involves solution of the coupled poro-elastic flow–structure

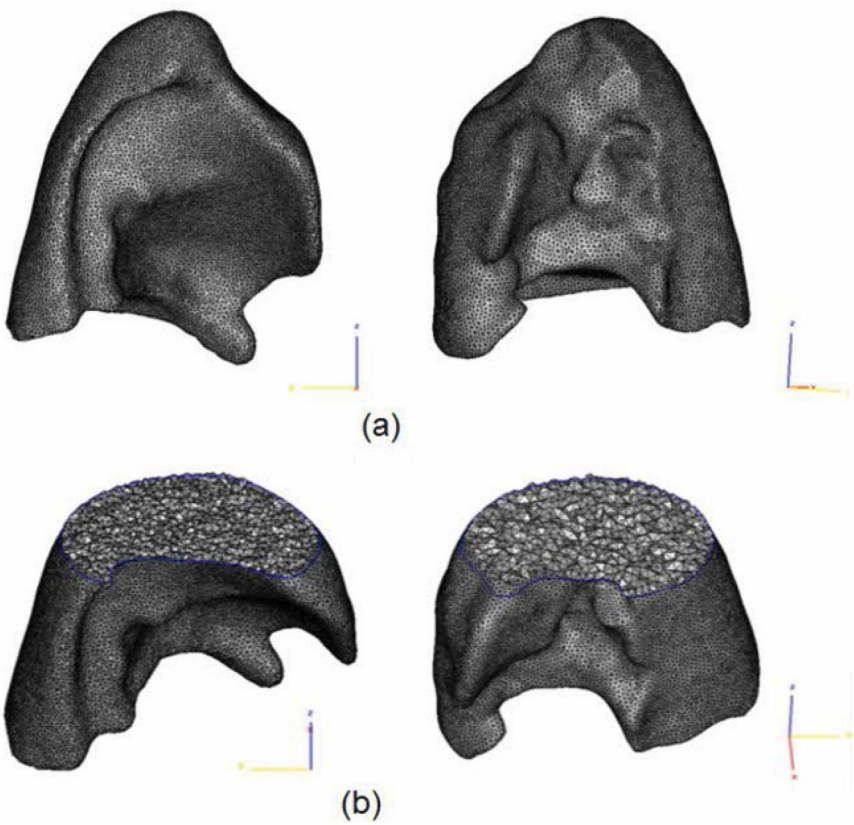

Fig. 1 Three dimensional lung shapes generated from 4D-CT scan: (*a*) surface meshes (*b*) cutout of a section of reconstructed lungs, typical computational volume meshes generated and applied in the finite-element model

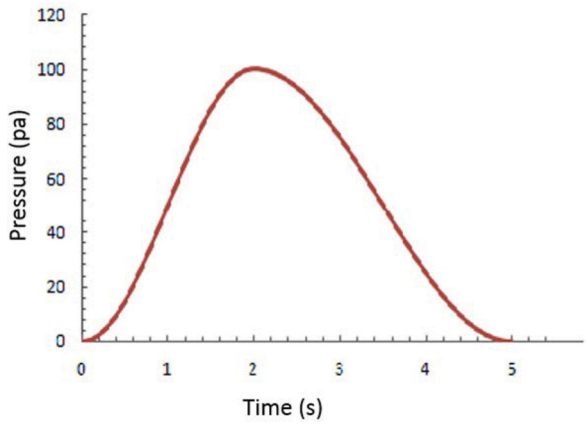

Fig. 2 Prescribe inlet pressure

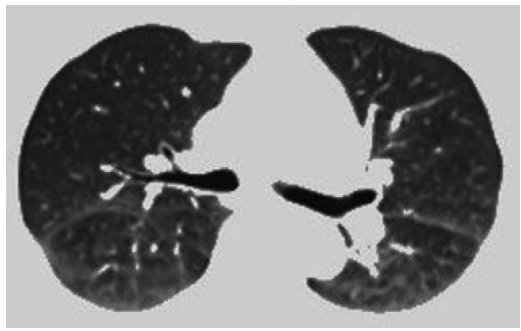

Fig. 3 3DCT lung anatomy used as the reference geometry for the CFD analysis

interaction sets of equations within the lung. The porosity represents the proportion of total volume (solid and fluid) which is occupied by the fluid and is defined as [17]

$$\varnothing = 1 - \frac{\mathbf{J}^0}{\mathbf{J}}\left(1 - \varnothing^0\right) \tag{3}$$

where $\mathbf{J}$ is the geometric element Jacobian and the superscript "0" indicates the quantities at initial reference configuration.

In contrast to the conventional fluid–structure interaction approach in which fluid and structural variables are coupled only at the interface, the present analysis allows coupling in the entire porous medium [17]. The microscopic fluid stress ($\boldsymbol{\sigma}_f \equiv -\mathrm{p}_f\mathbf{I}$) is added to the structural model as internal stress and displacement compatibility must be satisfied throughout the porous medium ($\mathbf{u}_f = \mathbf{u}_s = \mathbf{u}$) where $\mathbf{u}_f$ and $\mathbf{u}_s$ represent the fluid and solid displacement, respectively.

Assuming incompressible transient flow condition in the fluid domain, the pore fluid flows through the porous solid structure according to the Darcy's law [17], thus,

$$\frac{\mu_f}{\mathbf{K}} \cdot (\mathbf{v} - \mathbf{w}) + \nabla \mathrm{p}_f + \rho_f \boldsymbol{g} = 0 \tag{4}$$

where $\mathbf{K}$, μ_f, and ρ_f represent the permeability tensor, viscosity, and density of air, respectively, p_f is the local (pore) pressure, $\mathbf{v}$ is

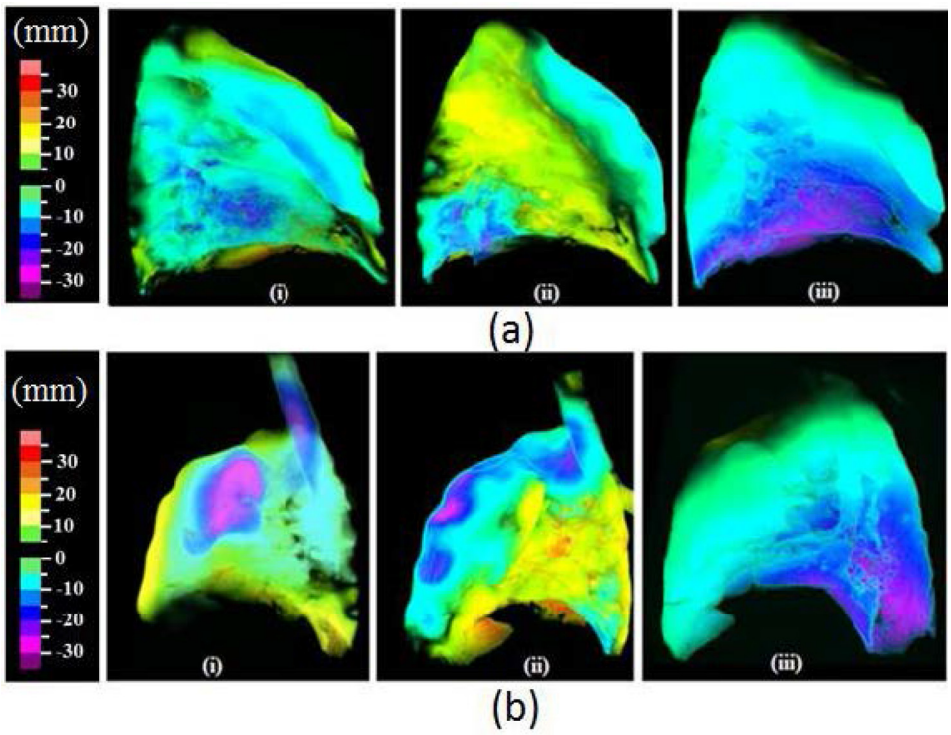

Fig. 4 Lung deformation along the (i) *x* axis, (ii) *y* axis, and (iii) *z* axis computed for the (*a*) left lung and (*b*) right lung using a multiresolution optical flow algorithm

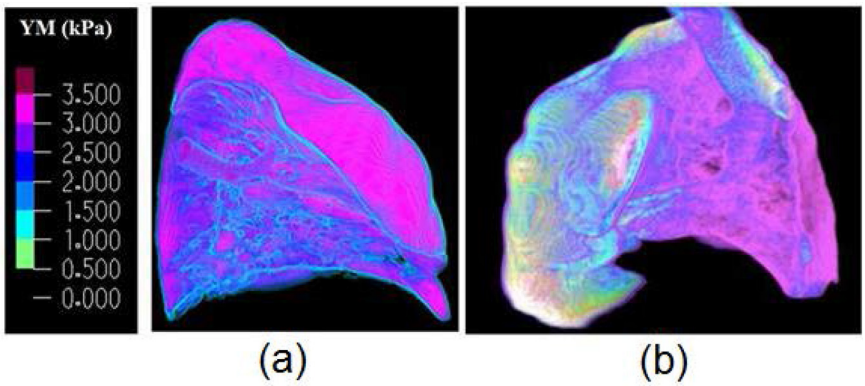

Fig. 5 Three-dimensional volume rendering of the YM values for the (*a*) right and (*b*) left lung obtained from the 4DCT lung registration and a linear deformation model

the air velocity vector, and **w** represents the moving mesh velocity vector. The displacement compatibility indicates that the moving mesh velocity is equal to the solid velocity ($\mathbf{w} = \dot{\mathbf{u}}$) throughout the porous medium. In the solid domain, the lung tissue is assumed to be linear isotropic elastic [18,19]. Note that the isentropic assumption is considered within each element and the YM varies from one element to another. The solid displacement is obtained by solving for the elastic displacement field, **u**, from the Navier's equation

$$G\nabla^2\mathbf{u} + \frac{G}{1-2\nu}\nabla(\nabla.\mathbf{u}) = \nabla p_f - \mathbf{b} \tag{5}$$

where G and ν are the tissue Shear modulus and Poisson ratio, respectively, and **b** is body force. The Shear modulus is related to the YM (E) through the relation $G = E/2(1+\nu)$.

Equations (4) and (5) are solved for the individual, specific patient lung geometry using the ADINA computational code [20] to predict spatial distribution of the lung displacement ($\mathbf{u} = \mathbf{f}_{\text{CFD}}$). This displacement is used as input in the fusion algorithm as described in Sec. 2.1.

2.3.4 Material Properties. The local elastic properties of the subject-specific lung are determined using an inverse noninvasive methodology [21]. The maximum YM obtained at the lower part of the lobe is 4.03 kPa for the left lung and 4.05 kPa for the right lung, while a minimum value of 0.01 kPa is obtained at the top for both lungs. The average YM obtained and used in the present study is 0.64 kPa for the left lung and 0.67 kPa for the right lung. These values fall within the range that has been used in other studies [22]. The heterogeneous YM values are implemented in the CFD model using in-house C code.

2.3.5 Input Data and Boundary Condition. The Poisson ratio ν is assumed to be 0.35, which falls within the range (0.25–0.47)

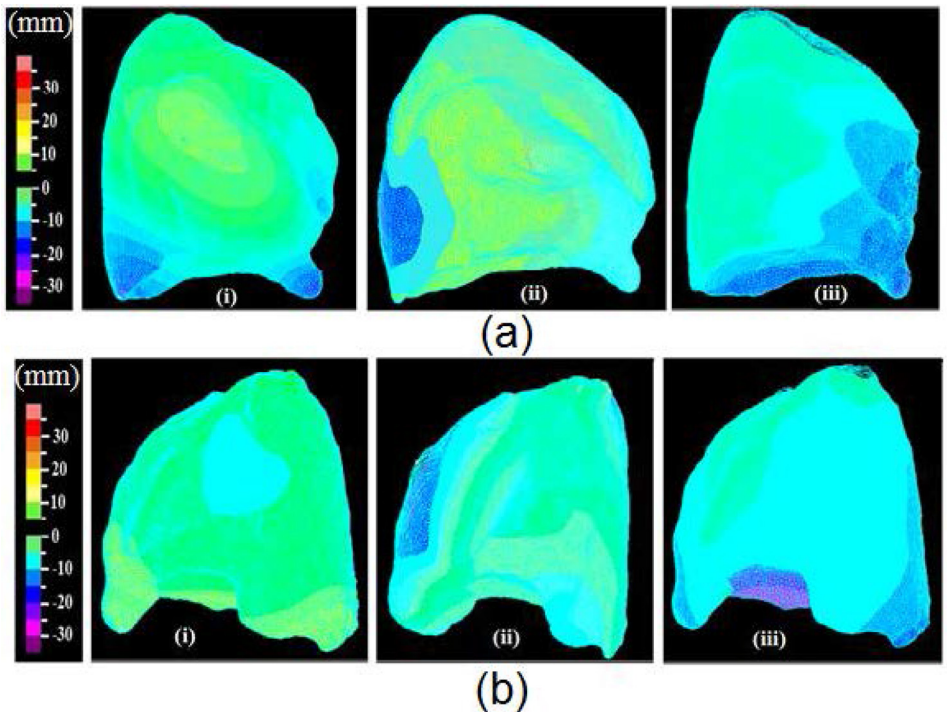

Fig. 6 Lung deformation along the (i) *x* axis, (ii) *y* axis, and (iii) *z* axis computed for the (*a*) left lung and (*b*) right lung using CFD model

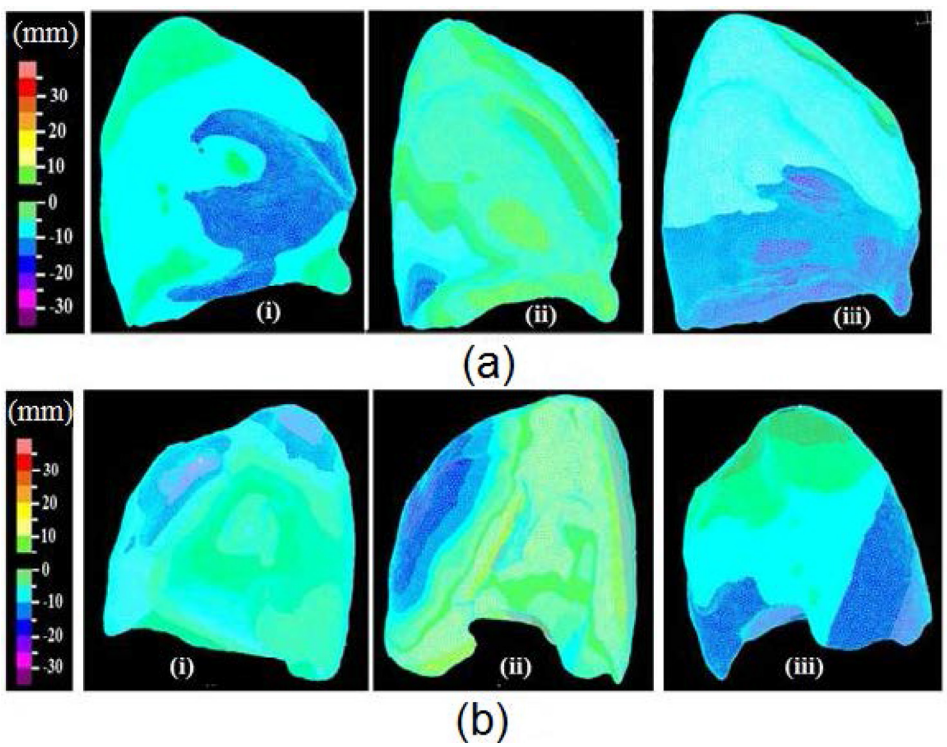

Fig. 7 Optimal lung deformation along the (i) *x* axis, (ii) *y* axis, and (iii) *z* axis computed for the (*a*) left lung and (*b*) right lung

suggested in previous studies [23]. The lung density is assumed to be 700 kg/m^3 [23].

The spatially dependent YM obtained in Sec. 2.3.4 is utilized in the model. The inlet is assumed to be at the hilum where the airway enters the lung, determined by the intersection of the trachea with the lung. Periodic pressure boundary condition is imposed at the inlet to the lobe as illustrated in Fig. 2 over one breathing cycle. The inlet pressure is assumed to reach its maximum value at $t = 2$ s at the end of the inhalation phase.

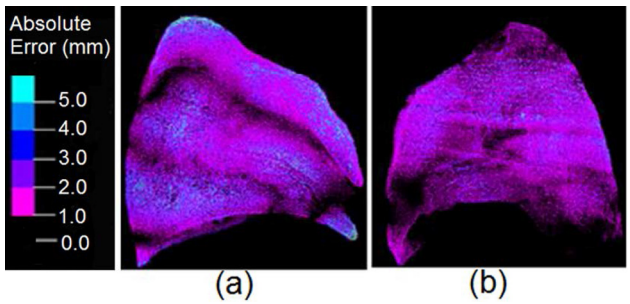

Fig. 8 Differences in the displacement observed between the optimal lung deformation and the deformation observed in the 4D-CT DIR is shown for left and right lungs

3 Results

The following presents the results obtained from the experiment and CFD model. These results are utilized in testing the current state of the fusion algorithm.

3.1 Image Registration Results. Figure 3 shows the CT slice of the lung anatomy at the end-expiration stage. This anatomy is used as the reference anatomy and the voxel deformation is computed for each voxel in the end-expiration stage by mapping to the end-inspiration stage.

Figure 4(*a*) depicts the 3D lung deformation computed using the 4D DIR for the left lung. The corresponding results for the right lung are presented in Fig. 4(*b*), illustrating the differences between the deformation of both lungs. Figures 5(*a*) and 5(*b*) show the 3D volume-rendered representation of the YM obtained from the linear elastic deformation model and the 4D lung DIR mechanism.

3.2 CFD Results. The predicted map of displacement using the porous flow–structure interaction model in x, y, and z directions (in mm) is plotted in Figs. 6(*a*) and 6(*b*) for the left and right lungs, respectively. The maximum and minimum displacements are presented for both lungs with variations between the two extremes.

3.3 Optimal Results From Fusion Algorithm. The fused displacement results obtained from fusion algorithm are used to calculate the spatially distributed optimal YM in an inverse manner. The value of the optimized YM is applied in the CFD model to obtain the optimal displacement. Figures 7(*a*) and 7(*b*) show the predicted map of the optimal CFD displacement in the x, y, and z directions (in mm) for the right and left lungs, respectively. The maximum and minimum displacements are presented for both lungs with variations between the two extremes.

3.4 Validation. Figures 8(*a*) and 8(*b*) show the discrepancy observed between the optimal lung deformation and the deformation observed in the 4DCT DIR. The results show that the discrepancies are less than 3 mm for most of the interior nodes and larger on the surface, particularly at the sharp edges of the lungs.

In order to investigate the effect of optimization in error reduction, the absolute displacement error for 15 selected landmark locations in both lungs are monitored and compared for both the CFD and optimal model. Table 1 compares the CFD simulation errors between the initial YM and optimal YM after the regularization. The DIR results are used as the gold standard to validate the results of the optimal CFD model.

Landmarks are selected at the interior, sharp edges and surfaces, identified by their x, y, z coordinates. The same coordinate system is used for the biomechanical model, 4DCT, and the fusion model. Therefore, having the x, y, z coordinates for each landmark, the same landmarks were chosen for comparison.

Figures 9(*a*) and 9(*b*) show the selected landmark locations (P1-P15) in the left and right lungs, respectively. Table 1 shows the absolute errors obtained from the standard CFD and optimal model for both lungs. The results for optimal model indicate a smaller error compared to the standard CFD model. The 95% confidence interval for the displacement error for the selected landmarks in both lungs is (3 ± 0.41) mm for the biomechanical model and (1.50 ± 0.46) mm for the optimal model. The landmarks on the surfaces and sharp edges are shown in gray while landmarks in the interior are shown in white in Table 1. Optimization results in a significant reduction in error for the interior landmarks. In the left lung, the average error for the landmarks on the surface and edges is reduced by 1.11 mm while this value is 2.96 mm for the interior nodes. In the right lung, the average displacement errors after optimization are reduced by 1.34 mm and 0.86 mm for the interior and surface nodes, respectively. These results show that although optimization is effective in reducing the displacement error at the surface nodes, it is more effective for the interior nodes.

Table 1 Discrepancy observed between the CFD (deformation) results using initial YM values and CFD (deformation) results using optimal YM values (mm) and the deformation observed in 4DCT DIR

Left lung			Right lung		
Nodes	Absolute error (mm)-CFD results using initial YM values	Absolute error (mm)-CFD results using optimal YM values	Nodes	Absolute error (mm)-CFD results using initial YM values	Absolute error (mm)-CFD results using optimal YM values
P1	3.5	3.2	P16	3.73	1.41
P2	3.68	2.19	P17	4.07	3.15
P3	4.39	4.03	P18	1.71	1.51
P4	2.5	0.22	P19	3.86	2.91
P5	4.92	1.49	P20	1.64	0.54
P6	4.5	0.28	P21	1.34	0.67
P7	3.3	0.011	P22	3.79	2.16
P8	3.3	2.03	P23	2.35	0.6
P9	4.5	0.51	P24	0.85	0.088
P10	2.11	0.51	P25	1.42	0.71
P11	2.98	2.6	P26	2.83	1.16
P12	1.83	0.43	P27	2.41	0.00
P13	4.03	4.00	P28	2.5	2.00
P14	3.8	0.28	P29	3.01	2.56
P15	4.09	3.5	P30	0.77	0.09

Landmarks on the surfaces and sharp edges are shown in gray.
Landmarks in the interior are shown in white.

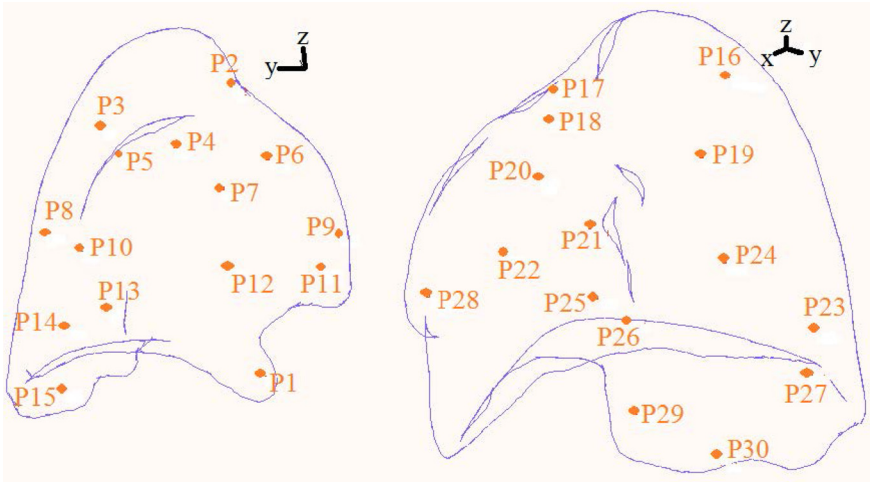

Fig. 9 Location of selected landmarks in (*a*) left and (*b*) right lung

4 Conclusion

An algorithm for fusing the quantitative DIR-based displacement and CFD-based fluid–structure interaction simulation data has been proposed. A description has been provided of how the biomechanical modeling outcomes can be combined with the DIR data using the theory of TR. The quantitative DIR-based data is obtained by means of 4DCT lung image registration algorithm to estimate the motion of the lung. A heterogeneous poro-elastic model is employed to obtain the CFD solution for lung deformation. The accuracy of the numerical solution is enhanced through fusion with the imaging data beyond the classical comparison between the two sets of data. Such a model will in the future be used for the development of improved lung anatomy models and motion tracking mechanisms that will ultimately lead to an optimal patient radiation-treatment simulator.

Although validation of the results discussed in Table 1 can prove the optimality of the regularization process, a phantom study would be ideal to systematically understand the regularization process. Such a lung phantom that is both compatible with the patient's observed physiology and airflow physics does not currently exist. The design of such physics-based multimodality consistent lung models would be desirable in a future study.

Future work will also integrate the ribcage and utilize nonlinear hyperelastic material property to enhance the accuracy of the biomechanical model. It should be noted that in spite of the linear elastic property used here, the model extends beyond previous studies by utilizing the material constants derived from real human patients. In contrast, most of the previous biomechanical modeling studies on human lung have assumed material constants obtained from experiments on animal tissue or cadaver, which are inadequate for human radiotherapy.

Acknowledgment

The work was funded in part by the National Science Foundation under Grant Nos. 1200579 and 1200841, and the Department of Radiation Oncology, University of California, Los Angeles. The authors acknowledge support of M.D. Anderson Cancer Center (Orlando), and useful discussion with Dr. Kupelian of UCLA Radiation Oncology.

Nomenclature

$\mathbf{b}$ = body force
$\mathbf{c}$ = optimal nodal value vectors
E = Young's modulus
$\mathbf{f}_{\text{CFD}}$ = CFD displacement
$\mathbf{f}_{\text{opt}}$ = optimal displacement
$\mathbf{f}_{\text{4DCT}}$ = 4DCT displacement
$\mathbf{g}$ = gravity vector
G = Shear modulus
$\mathbf{h}, \mathbf{l}_e, \mathbf{m}, \mathbf{n}_e, \mathbf{o}, \mathbf{p}_e, \mathbf{q}_e, \mathbf{t}$ = interpolation functions
$\mathbf{I}$ = identity matrix
$\mathbf{J}$ = geometric element Jacobian
$\mathbf{K}$ = permeability tensor
p_f = the local (pore) pressure
q = number of nodes
$\mathbf{R}$ = the SO(3) rotation group matrix
$\mathbf{S}$ = expansion of the SO(3) rotation group matrix in 3D
$\mathbf{u}$ = lung displacement vector
$\mathbf{v}$ = air velocity vector
$\mathbf{w}$ = moving mesh velocity vector
$\mathbf{Y}$ = HSH transform
$\mathbf{z}$ = objective functional
α = regularization parameter
$\boldsymbol{\gamma}$ = CFD nodal value vectors
δ = Dirac delta function
$\boldsymbol{\varepsilon}$ = discrepancy between optimal and 4DCT displacement
(θ, φ, χ) = hyperspherical coordinate
μ_f = air viscosity
ν = Poisson ratio
ρ_f = density of air
$\boldsymbol{\sigma}_f$ = fluid stress
$\boldsymbol{\omega}$ = regularization operator
$\varnothing$ = porosity

Subscripts

CFD = CFD value
e = element defined variable
opt = optimal value
$\lambda,\ l,\ m, n$ = HSH coefficients
0 = coordinate origin
4DCT = 4DCT value

Superscripts

e = element defined variable
0 = initial reference configuration

Appendix: Numerical Solution of the Objective Functional

The functions in Eq. (2) are defined based on the nodal values. For each element, consider $e = 1, 2, \ldots, q$; q represents the number of nodes and $\mathbf{c}(\mathbf{x}_e)$ and $\boldsymbol{\gamma}(\mathbf{x}_e)$ are the optimal and CFD nodal value vectors, respectively. Then within each element, the optimal and CFD functions are defined, respectively, as

$$\mathbf{f}_{\text{opt}}(\mathbf{x}) = \sum_{e=0}^{q} \mathbf{h}(\mathbf{x},\ \mathbf{x}_e)\mathbf{c}(\mathbf{x}_e) \tag{A1}$$

$$\mathbf{f}_{\text{CFD}}(\mathbf{x}) = \sum_{e=0}^{q} \mathbf{h}(\mathbf{x},\ \mathbf{x}_e)\boldsymbol{\gamma}(\mathbf{x}_e) \tag{A2}$$

In the above equations , $\mathbf{h}(\mathbf{x},\ \mathbf{x}_e)$ is the interpolation function. The optimal and CFD functions are in fact the sum over all nodal values in the element. By defining the optimal and CFD functions in terms of nodal values, the next step is to substitute these functions in Eq. (2) and differentiate with respect to nodal values to find the minimum objective functional in each element

$$\begin{aligned}\mathbf{z} = \frac{1}{2}\alpha\ &\left[\mathbf{f}_{4\text{DCT}}(\mathbf{x}) - \sum_{e=0}^{q} \mathbf{h}(\mathbf{x},\ \mathbf{x}_e)\mathbf{c}(\mathbf{x}_e)\right]^2 \\ &+ \frac{1}{2}\sum_{e=0}^{q} \mathbf{h}^2(\mathbf{x},\ \mathbf{x}_e)\ [\mathbf{c}(\mathbf{x}_e) - \boldsymbol{\gamma}(\mathbf{x}_e)]^2 \\ &+ \frac{1}{2}\sum_{e=0}^{q} \mathbf{o}^2(\mathbf{x},\ \mathbf{x}_e)\ [\mathbf{c}(\mathbf{x}_e) - \boldsymbol{\gamma}(\mathbf{x}_e)]^2 \\ &+ \frac{1}{2}\sum_{e=0}^{q} \mathbf{t}^2(\mathbf{x},\ \mathbf{x}_e)\ [\mathbf{c}(\mathbf{x}_e) - \boldsymbol{\gamma}(\mathbf{x}_e)]^2 \\ &+ \frac{1}{2}\sum_{e=0}^{q} \mathbf{m}^2(\mathbf{x},\ \mathbf{x}_e)\ [\mathbf{c}(\mathbf{x}_e) - \boldsymbol{\gamma}(\mathbf{x}_e)]^2\end{aligned} \tag{A3}$$

where $\mathbf{o}$, $\mathbf{t}$, and $\mathbf{m}$ are new interpolation functions, defined as $\partial\mathbf{h}(\mathbf{x},\mathbf{x}_e)/\partial\text{x}$, $\partial\mathbf{h}(\mathbf{x},\mathbf{x}_e)/\partial\text{y}$, and $\partial\mathbf{h}(\mathbf{x},\mathbf{x}_e)/\partial\text{z}$, respectively.

Differentiating Eq. (A3) with respect to $\mathbf{c}(\mathbf{x}_e)$

$$\begin{aligned}\frac{\partial \mathbf{z}}{\partial \mathbf{c}(\mathbf{x}_e)} = \tau^e\alpha\ &\left[\mathbf{f}_{4\text{DCT}}(\mathbf{x}) - \sum_{e=0}^{q} \mathbf{h}(\mathbf{x},\ \mathbf{x}_e)\mathbf{c}(\mathbf{x}_e)\right]\left[-\mathbf{l}_e(\mathbf{x},\mathbf{x}_e) + \sum_{e=0}^{q} \mathbf{h}(\mathbf{x},\ \mathbf{x}_e)\mathbf{l}_e(\mathbf{x},\mathbf{x}_e)\ \left[\mathbf{c}(\mathbf{x}_e) - \boldsymbol{\gamma}(\mathbf{x}_e)\right]\right] \\ &+ \sum_{e=0}^{q} \mathbf{o}(\mathbf{x},\ \mathbf{x}_e)\mathbf{n}_e(\mathbf{x},\mathbf{x}_e)\ \left[\mathbf{c}(\mathbf{x}_e) - \boldsymbol{\gamma}(\mathbf{x}_e)\right] + \sum_{e=0}^{q} \mathbf{t}(\mathbf{x},\ \mathbf{x}_e)\ \mathbf{p}_e(\mathbf{x},\mathbf{x}_e)\left[\mathbf{c}(\mathbf{x}_e) - \boldsymbol{\gamma}(\mathbf{x}_e)\right] + \sum_{e=0}^{q} \mathbf{m}(\mathbf{x},\ \mathbf{x}_e)\ \mathbf{q}_e(\mathbf{x},\mathbf{x}_e)\left[\mathbf{c}(\mathbf{x}_e) - \boldsymbol{\gamma}(\mathbf{x}_e)\right]\end{aligned} \tag{A4}$$

where $\mathbf{l}_e(\mathbf{x},\mathbf{x}_e) = \partial\mathbf{h}(\mathbf{x},\mathbf{x}_e)/\partial\mathbf{c}(\mathbf{x}_e)$, $\mathbf{n}_e(\mathbf{x},\mathbf{x}_e) = \partial\mathbf{o}_e(\mathbf{x},\mathbf{x}_e)/\partial\mathbf{c}(\mathbf{x}_e)$, $\mathbf{p}_e(\mathbf{x},\mathbf{x}_e) = \partial\mathbf{t}_e(\mathbf{x},\mathbf{x}_e)/\partial\mathbf{c}(\mathbf{x}_e)$, and $\mathbf{q}_e(\mathbf{x},\mathbf{x}_e) = \partial\mathbf{m}_e(\mathbf{x},\mathbf{x}_e)/\partial\mathbf{c}(\mathbf{x}_e)$.

The parameter τ^e is an indicator of whether or not imaging data exist in the current element [12]. If no imaging data exists in the element the value of τ^e becomes zero and the first integral in Eq. (A4) is eliminated, otherwise the value of τ^e is set to unity (1).

Minimizing the equation by setting the LHS of Eq. (A4) to zero,

$$\begin{aligned}\text{Let } \mathbf{d}(\mathbf{x},\mathbf{x}_e) = &\mathbf{h}(\mathbf{x},\mathbf{x}_e)\mathbf{l}_e(\mathbf{x},\mathbf{x}_e) + \mathbf{o}(\mathbf{x},\mathbf{x}_e)\mathbf{n}_e(\mathbf{x},\mathbf{x}_e) \\ &+ \mathbf{t}(\mathbf{x},\mathbf{x}_e)\mathbf{p}_e(\mathbf{x},\mathbf{x}_e) + \mathbf{m}(\mathbf{x},\mathbf{x}_e)\mathbf{q}_e(\mathbf{x},\mathbf{x}_e)\end{aligned} \tag{A5}$$

$$\begin{aligned}0 = \tau^e\alpha\ &[\mathbf{f}_{4\text{DCT}}(\mathbf{x}) + \sum_{e=0}^{q} \mathbf{h}(\mathbf{x},\ \mathbf{x}_e)\mathbf{c}(\mathbf{x}_e)\mathbf{l}_e(\mathbf{x},\mathbf{x}_e)] \\ &+ \sum_{e=0}^{q} \mathbf{d}(\mathbf{x},\mathbf{x}_e\ )\ [\mathbf{c}(\mathbf{x}_e) - \boldsymbol{\gamma}(\mathbf{x}_e)]\end{aligned} \tag{A6}$$

The equation can be further simplified as

$$\begin{aligned}0 = \tau^e\alpha &\left[\mathbf{f}_{4\text{DCT}}(\mathbf{x}) + \sum_{e=0}^{q} \mathbf{h}\mathbf{l}_e(\mathbf{x},\mathbf{x}_e)\mathbf{c}(\mathbf{x}_e)\right] \\ &+ \sum_{e=0}^{q} \mathbf{d}(\mathbf{x},\mathbf{x}_e)[\mathbf{c}(\mathbf{x}_e) - \boldsymbol{\gamma}(\mathbf{x}_e)]\end{aligned} \tag{A7}$$

Let

$$\mathbf{d}'(\mathbf{x},\mathbf{x}_e) = \mathbf{d}(\mathbf{x},\mathbf{x}_e) + \tau^e\ \alpha\ \mathbf{h}\ \mathbf{l}_e(\mathbf{x},\mathbf{x}_e) \tag{A8}$$

$$0 = \tau^e\alpha\ \mathbf{f}_{4\text{DCT}}(\mathbf{x}) + \sum_{e=0}^{q} \mathbf{d}'(\mathbf{x},\mathbf{x}_e)\mathbf{c}(\mathbf{x}_e) - \sum_{e=0}^{q} \mathbf{d}(\mathbf{x},\mathbf{x}_e)\boldsymbol{\gamma}(\mathbf{x}_e) \tag{A9}$$

$$\sum_{e=0}^{q} \mathbf{d}'(\mathbf{x},\mathbf{x}_e)\mathbf{c}(\mathbf{x}_e) = \sum_{e=0}^{q} \mathbf{d}(\mathbf{x},\mathbf{x}_e)\boldsymbol{\gamma}(\mathbf{x}_e) - \tau^e\ \alpha\ \mathbf{f}_{4\text{DCT}}(\mathbf{x}) \tag{A10}$$

Now, we have two convolutions in a discrete domain on either side of the formulation, thus hyperspherical harmonic (HSH) transformations are applied on either side of Eq. (A10) to get the following relation for $\mathbf{c}(\mathbf{x}_e)$. As a first step toward this process, we rewrite the $\mathbf{c}(\mathbf{x}_e)$ and $\boldsymbol{\gamma}(\mathbf{x}_e)$ using hyperspherical coordinates with a rotational invariant notation as follows [21]:

$$\mathbf{c}(\mathbf{x}_e) = \mathbf{c}(\mathbf{r}_{(\theta_e,\varphi_e,\chi_e)}(\theta_0,\varphi_0,\chi_0)) \tag{A11}$$

$$\boldsymbol{\gamma}(\mathbf{x}_e) = \boldsymbol{\gamma}(\mathbf{r}_{(\theta_e,\varphi_e,\chi_e)}(\theta_0,\varphi_0,\chi_0)) \tag{A12}$$

In the above two equations, $(\theta_e,\varphi_e,\chi_e)$ represents the coordinate system for $\mathbf{x}_e$ and $(\theta_0,\varphi_0,\chi_0)$ represents the coordinate origin. The term $\mathbf{r}_{(\theta_e,\varphi_e,\chi_e)}(\theta_0,\varphi_0,\chi_0)$ represents the SO(3) group rotation of the origin $(\theta_0,\varphi_0,\chi_0)$ by the angle $(\theta_e,\varphi_e,\chi_e)$. Such a group rotation term enables us to define Eqs. (A11) and (A12) in terms of the origin and then subsequently rotate the origin to the location given by $(\theta_e,\varphi_e,\chi_e)$. We now expand the formulation in Eqs. (A11) and (A12) using HSH transformation thus

$$\begin{aligned}\mathbf{c}(\mathbf{R}_{(\theta_e,\varphi_e,\chi_e)}(\theta_0,\varphi_0,\chi_0)) = &\sum_{\lambda_1}\sum_{l_1}\sum_{m_1}\sum_{n_1} \mathbf{c}_{\lambda_1 l_1 m_1}\ \mathbf{Y}_{l_1 n_1}\ \mathbf{S}_{\lambda_1 m_1 n_1} \\ &\times (\theta_e,\varphi_e,\chi_e)\end{aligned} \tag{A13}$$

$$\begin{aligned}\boldsymbol{\gamma}(\mathbf{R}_{(\theta_e,\varphi_e,\chi_e)}(\theta_0,\varphi_0,\chi_0)) = &\sum_{\lambda_1}\sum_{l_1}\sum_{m_1}\sum_{n_1} \boldsymbol{\gamma}_{\lambda_1 l_1 m_1}\ \mathbf{Y}_{\lambda_1 l_1 m_1}\ \mathbf{S}_{\lambda_1 m_1 n_1} \\ &\times (\theta_e,\varphi_e,\chi_e)\end{aligned} \tag{A14}$$

In the above two equations, the term $\mathbf{S}_{\lambda_1 m_1 n_1}(\theta_e, \varphi_e, \chi_e)$ refers to the 3D HSH transformation of the SO(3) rotation and $\mathbf{Y}_{\lambda_1 l_1 n_1}$ represents the HSH transformation of the input data. For detailed definition of these terms, see Ref. [21]. We now expand $\mathbf{d}$ and $\mathbf{d}'$ using HSH transformation as follows:

$$\mathbf{d}(\theta, \varphi, \chi, \theta_e, \varphi_e, \chi_e) = \sum_{\lambda_2} \sum_{l_2} \sum_{\lambda_2'} \sum_{l_2'} \sum_{m_2'} \mathbf{d}_{\lambda_2 l_2 \lambda_2' l_2' m_2'} \times (\mathbf{Y}^*{}_{\lambda_2 l_2 m_2'}(\theta_e, \varphi_e, \chi_e)) \mathbf{Y}_{\lambda_2' l_2' m_2'}(\theta, \varphi, \chi) \tag{A15}$$

$$\mathbf{d}'(\theta, \varphi, \chi, \theta_e, \varphi_e, \chi_e) = \sum_{\lambda_2} \sum_{l_2} \sum_{\lambda_2'} \sum_{l_2'} \sum_{m_2'} \mathbf{d}'_{\lambda_2 l_2 \lambda_2' l_2' m_2'} \times (\mathbf{Y}^*{}_{\lambda_2 l_2 m_2'}(\theta_e, \varphi_e, \chi_e)) \mathbf{Y}_{\lambda_2' l_2' m_2'}(\theta, \varphi, \chi) \tag{A16}$$

The term $\tau^e \alpha\ \mathbf{f}_{4\mathrm{DCT}}(\mathbf{x})$, which is on the RHS of Eq. (A10) can be expanded as

$$\tau^e \alpha\ \mathbf{f}_{4\mathrm{DCT}}(\theta, \varphi, \chi) = \sum_{\lambda} \sum_{l} \sum_{m} \tau^e \alpha\ \mathbf{f}_{4\mathrm{DCT}}(\theta, \varphi, \chi) \delta(\lambda) \delta(l) \delta(m) \tag{A17}$$

where δ is the Dirac delta function.

The first term of the RHS of Eq. (A10) can be expanded as

$$\sum_{\lambda_1} \sum_{l_1} \sum_{m_1} \sum_{n_1} \sum_{\lambda_2} \sum_{l_2} \sum_{\lambda_2'} \sum_{l_2'} \sum_{m_2'} \boldsymbol{\gamma}_{\lambda_1 l_1 m_1} \mathbf{d}_{\lambda_2 l_2 \lambda_2' l_2' m_2'} \mathbf{S}_{\lambda_1 m_1 n_1} \times (\theta_e, \varphi_e, \chi_e) \mathbf{Y}_{Y l_2' m_2'}(\theta_0, \varphi_0, \chi_0) \mathbf{B}_{\lambda_1 l_1 n_1 \lambda_2' l_2' m_2'} \tag{A18}$$

where

$$\mathbf{B}_{\lambda_1 l_1 n_1 \lambda_2' l_2' m_2'} = \delta_{\lambda_1 \lambda_2'} \quad \delta_{l_1 l_2'} \quad \delta_{n_1 m_2'} \tag{A19}$$

The term can be further simplified as

$$\sum_{\lambda_1} \sum_{l_1} \sum_{m_1} \sum_{\lambda_2} \sum_{l_2} \sum_{m_2} \boldsymbol{\gamma}_{\lambda_1 l_1 m_1} \mathbf{d}_{\lambda_1 l_1 \lambda_2 l_2 n_1} \mathbf{S}_{\lambda_1 m_1 n_1}(\theta_e, \varphi_e, \chi_e) \times \mathbf{Y}_{\lambda_2' l_2' n_1}(\theta_0, \varphi_0, \chi_0) + Q(\theta, \varphi, \chi) \tag{A20}$$

where $Q(\theta, \varphi, \chi)$ is a constant term.

Similarly the LHS of Eq. (A10) can be simplified using HSH transformation

$$\sum_{\lambda_1} \sum_{l_1} \sum_{m_1} \sum_{\lambda_2} \sum_{l_2} \sum_{n_1} \mathbf{c}_{\lambda_1 l_1 m_1} \mathbf{d}'_{\lambda_1 l_1 \lambda_2 l_2 n_1} \mathbf{S}_{\lambda_1 m_1 n_1}(\theta_e, \varphi_e, \chi_e) \times \mathbf{Y}_{l_2' n_1}(\theta_0, \varphi_0, \chi_0) \tag{A21}$$

Equating the frequency coefficients for $\lambda_1 l_1 m_1 \neq 0$ we get

$$\mathbf{c}_{\lambda_1 l_1 m_1} = \frac{\sum_{\lambda_2} \sum_{l_2} \sum_{n_1} \mathbf{d}'_{\lambda_1 l_1 \lambda_2 l_2 n_1} * \ \boldsymbol{\gamma}_{\lambda_1 l_1 m_1}}{\sum_{\lambda_2} \sum_{l_2} \sum_{n_1} \mathbf{d}_{\lambda_1 l_1 \lambda_2 l_2 n_1}} \tag{A22}$$

and for $\lambda_1 l_1 m_1 = 0$ we get

$$\mathbf{c}_{000} = \frac{\sum_{\lambda_2} \sum_{l_2} \sum_{n_1} \mathbf{d}'_{00 \lambda_2 l_2 n_1} * \ \boldsymbol{\gamma}_{000} + [\mathrm{constant}\ Q(\theta, \varphi, \chi)]}{\sum_{\lambda_2} \sum_{l_2} \sum_{n_1} \mathbf{d}_{00 \lambda_2 l_2 n_1}} \tag{A23}$$

It can be seen that the formulation is analytical in nature, i.e., for known values of $\mathbf{f}_{4\mathrm{DCT}}$ and the subsequent nodal values of the CFD analysis, $\mathbf{c}_{\lambda_1 l_1 m_1}$ can be calculated and ultimately the $\mathbf{f}_{\mathrm{opt}}$ can be estimated. The formulation by itself is a noniterative direct solution.

References

[1] Keall, P. J., Mageras, G. S., Balter, J. M., Emery, R. S., Forster, K. M., Jiang, S. B., Kapatoes, J. M., Low, D. A., Murphy, M. J., and Murray, B. R., 2006, "The Management of Respiratory Motion in Radiation Oncology Report of AAPM Task Group 76," Med. Phys., **33**(10), pp. 3874–3938.

[2] Santhanam, A. P., Min, Y., Rolland, J. P., Imielinska, C., and Kupelian, P. A., 2011, "Four-Dimensional Computed Tomography Lung Registration Methods," *Lung Imaging and Computer Aided Diagnosis*, A. EI-Baz and J. S. Suri, eds., CRC Press, Boca Raton, FL, pp. 85–108.

[3] Plathow, C., Ley, S., Fink, C., Puderbach, M., Hosch, W., Schmähl, A., Debus, J., and Kauczor, H.-U., 2004, "Analysis of Intrathoracic Tumor Mobility During Whole Breathing Cycle by Dynamic MRI," Int. J. Radiat. Oncol., **59**(4), pp. 952–959.

[4] Ilegbusi, O. J., Seyfi, B., and Salvin, R., 2013, "Patient-Specific Model of Lung Deformation Using Spatially Dependent Constitutive Parameters," Math. Comput. Modell. Dyn., **20**(6), pp. 546–556.

[5] Al-Mayah, A., Moseley, J., and Brock, K., 2008, "Contact Surface and Material Nonlinearity Modeling of Human Lungs," Phys. Med. Biol., **53**(1), pp. 305–317.

[6] Ilegbusi, O. J., Li, Z., Seyfi, B., Min, Y., Meeks, S., Kupelian, P., and Santhanam, A. P., 2012, "Modeling Airflow Using Subject-Specific 4DCT-Based Deformable Volumetric Lung Models," J. Biomed. Imaging, **2012**, pp. 4–14.

[7] Seyfi, B., Santhanam, A. P., and Ilegbusi, O. J., "Application of Fusion Algorithm to Human Lung Dynamics," ASME Paper No. IMECE2012-86407.

[8] Brock, K., Sharpe, M., Dawson, L., Kim, S., and Jaffray, D., 2005, "Accuracy of Finite Element Model-Based Multi-Organ Deformable Image Registration," Med. Phys., **32**(6), pp. 1647–1695.

[9] Werner, R., Ehrhardt, J., Schmidt, R., and Handels, H., "Modeling Respiratory Lung Motion: A Biophysical Approach Using Finite Element Methods," Proc. SPIE, **6916**, p. 69160N.

[10] Eom, J., Xu, X. G., De, S., and Shi, C., 2010, "Predictive Modeling of Lung Motion Over the Entire Respiratory Cycle Using Measured Pressure-Volume Data, 4DCT Images, and Finite-Element Analysis," Med. Phys., **37**(8), pp. 4389–4423.

[11] Chang, J. Y., "Guidelines and Techniques for Image-Guided Radiotherapy for Non-Small Cell Lung Cancer," *Image-Guided Radiotherapy of Lung Cancer*, J. D. Cox, J. Y. Chang, and R. Komaki, eds., CRC Press, Boca Raton, FL, p. 25.

[12] Tikhonov, A. N., and Arsenin, V. Y., 1977, *Solutions of Ill-Posed Problems*, Winston, Halsted Press, Washington, NY.

[13] Vaina, L. M., Beardsley, S. A., and Rushton, S. K., 2004, *Optic Flow and Beyond*, Springer, Dordrecht.

[14] Min, Y., Neylon, J., Shah, A., Meeks, S., Lee, P., Kupelian, P., and Santhanam, A. P., 2014, "4D-CT Lung Registration Using Anatomy-Based Multi-Level Multi-Resolution Optical Flow Analysis and Thin-Plate Splines," Int. J. Comput. Assisted Radiol. Surg., **9**(5), pp. 875–889.

[15] Materialise, 2013, "Mimics® 13.1, Medical Image Segmentation for Engineering on AnatomyTM," Materialise HQ, Leuven, Belgium, http://www.biomedical. materialise.com/mimics

[16] Materialise, 2013, "3-matic® 5.01, 3-matic puts the 'Engineering' in Engineering on Anatomy™," Materialise HQ, Leuven, Belgium, http://biomedical.materialise.com/3-matic-0

[17] Zhang, H., Zhang, X., Ji, S., Guo, Y., Ledezma, G., Elabbasi, N., and deCougny, H., 2003, "Recent Development of Fluid–Structure Interaction Capabilities in the Adina System," Comput. Struct., **81**(8), pp. 1071–1085.

[18] Sobin, S., Fung, Y., and Tremer, H., 1988, "Collagen and Elastin Fibers in Human Pulmonary Alveolar Walls," J. Appl. Physiol., **64**(4), pp. 1659–1675.

[19] Toshima, M., Ohtani, Y., and Ohtani, O., 2004, "Three-Dimensional Architecture of Elastin and Collagen Fiber Networks in the Human and Rat Lung," Arch. Histol. Cytol., **67**(1), pp. 31–40.

[20] ADINA, 2013, "ADINA 9.0: Automatic Dynamic Incremental Nonlinear Analysis," ADINA R&D Inc., Watertown, MA, http://www.adina.com

[21] Santhanam, A. P., Min, Y., Mudur, S. P., Rastogi, A., Ruddy, B. H., Shah, A., Divo, E., Kassab, A., Rolland, J. P., and Kupelian, P., 2010, "An Inverse Hyper-Spherical Harmonics-Based Formulation for Reconstructing 3d Volumetric Lung Deformations," C. R. Méc., **338**(7), pp. 461–473.

[22] Villard, P.-F., Beuve, M., Shariat, B., Baudet, V., and Jaillet, F., 2005, "Simulation of Lung Behaviour With Finite Elements: Influence of Bio-Mechanical Parameters," Third International Conference on Medical Information Visualisation–Biomedical Visualisation (MediVis 2005), London, July 5–7, pp. 9–14.

[23] Chhatkuli, S., Koshizuka, S., and Uesaka, M., 2009, "Dynamic Tracking of Lung Deformation During Breathing by Using Particle Method," Model. Simul. Eng., **2009**, pp. 7–14.